Bioactive Materials 37 (2024) 505–516

Contents lists available at ScienceDirect

Bioactive Materials

journal homepage: www.keaipublishing.com/en/journals/bioactive-materials

Cryomicroneedle delivery of nanogold-engineered *Rhodospirillum rubrum* for photochemical transformation and tumor optical biotherapy

Qingxia Shi [a,b,1], Ting Yin [b,1], Cuiping Zeng [c,1], Hong Pan [a], Ze Chen [a], Lin Wang [c], Bo Wang [c,**], Mingbin Zheng [a,b,d,***], Lintao Cai [a,e,*]

[a] Guangdong Key Laboratory of Nanomedicine, CAS-HK Joint Lab of Biomaterials, Shenzhen Engineering Laboratory of Nanomedicine and Nanoformulations, Institute of Biomedicine and Biotechnology, Shenzhen Institute of Advanced Technology (SIAT), Chinese Academy of Sciences, Shenzhen, 518055, China
[b] Guangdong Key Laboratory for Research and Development of Natural Drugs, Key Laboratory for Nanomedicine, Guangdong Medical University, Dongguan, 523808, China
[c] CAS Key Laboratory of Quantitative Engineering Biology Shenzhen Institute of Synthetic Biology Shenzhen Institutes of Advanced Technology Chinese Academy of Sciences, Shenzhen, 518055, China
[d] National Clinical Research Center for Infectious Disease, Shenzhen Third People's Hospital, The Second Affiliated Hospital, Southern University of Science and Technology, Shenzhen, 518112, China
[e] Sino-Euro Center of Biomedicine and Health, Shenzhen, 518024, China

ARTICLE INFO

Keywords:
Cryomicroneedles
Photosynthetic bacteria
Lactate depletion
Hydrogen generation
Optical biotherapy

ABSTRACT

Tumor metabolite regulation is intricately linked to cancer progression. Because lactate is a characteristic metabolite of the tumor microenvironment (TME), it supports tumor progression and drives immunosuppression. In this study, we presented a strategy for antitumor therapy by developing a nanogold-engineered *Rhodospirillum rubrum* (R.r-Au) that consumed lactate and produced hydrogen for optical biotherapy. We leveraged a cryogenic micromolding approach to construct a transdermal therapeutic cryomicroneedles (CryoMNs) patch integrated with R.r-Au to efficiently deliver living bacterial drugs. Our long-term storage studies revealed that the viability of R.r-Au in CryoMNs remained above 90%. We found that the CryoMNs patch was mechanically strong and could be inserted into mouse skin. In addition, it rapidly dissolved after administering bacterial drugs and did not produce by-products. Under laser irradiation, R.r-Au effectively enhanced electron transfer through Au NPs actuation into the photosynthetic system of *R. rubrum* and enlarged lactate consumption and hydrogen production, thus leading to an improved tumor immune activation. Our study demonstrated the potential of CryoMNs-R.r-Au patch as a minimally invasive *in situ* delivery approach for living bacterial drugs. This research opens up new avenues for nanoengineering bacteria to transform tumor metabolites into effective substances for tumor optical biotherapy.

1. Introduction

The regulation of tumor microenvironment (TME) is critical to tumor regression because the tumor cell behaviors of proliferation, invasion, and metastatic spread are promoted throughout cancer progression. Notably, the accumulated extracellular lactate as the product of aerobic glycolysis is a universal hallmark of cancers among the complex metabolic pathways of tumors, which is a primary cause of an acidic tumor

Peer review under responsibility of KeAi Communications Co., Ltd.

* Corresponding author. Guangdong Key Laboratory of Nanomedicine, CAS-HK Joint Lab of Biomaterials, Shenzhen Engineering Laboratory of Nanomedicine and Nanoformulations, Institute of Biomedicine and Biotechnology, Shenzhen Institute of Advanced Technology (SIAT), Chinese Academy of Sciences, Shenzhen, 518055, China.
** Corresponding author.
*** Corresponding author. Guangdong Key Laboratory of Nanomedicine, CAS-HK Joint Lab of Biomaterials, Shenzhen Engineering Laboratory of Nanomedicine and Nanoformulations, Institute of Biomedicine and Biotechnology, Shenzhen Institute of Advanced Technology (SIAT), Chinese Academy of Sciences, Shenzhen, 518055, China.
E-mail addresses: bo.wang@siat.ac.cn (B. Wang), mb.zheng@siat.ac.cn (M. Zheng), lt.cai@siat.ac.cn (L. Cai).
[1] These authors contributed equally to this work.

https://doi.org/10.1016/j.bioactmat.2024.03.032
Received 26 November 2023; Received in revised form 27 March 2024; Accepted 28 March 2024

microenvironment (TME) [1,2].A weak acidic environment can threaten the survival of immune cells and can make cancer treatment less effective [3,4]. Accumulated evidence has verified that lactate is not only a acidic by-product of the metabolism of cancer cells, but also an important regulator of TME immunosuppression, leading to tumor progression [5,6]. Consequently, lactate-targeted therapy has emerged as a reliable and effective approach to effectively suppress tumor progression, such as suppressing lactate transport, depleting lactate in tumors, and inhibiting lactate generation. Targeted lactate therapeutic strategies include suppressing lactate transport, depleting lactate in tumors, and inhibiting lactate generation [7]. Significant challenges remain, however, despite the effectiveness of these strategies. Unsatisfactory therapeutic outcomes or off-target side effects may result from unfavorable pharmacokinetic conditions, including poor bioavailability or solubility and the specificity of small-molecule inhibitors, nucleic acids, and chemical drugs [8]. Therefore, it is essential to develop a good biocompatible and highly specific lactate-targeted therapy strategy.

Substantial efforts have been made to tackle these challenges by designing an intelligent depletion lactate system with biomimetic and biocompatible materials [9]. Inspired by nature, some living bacteria, because of their inherent bioactive behaviors and physiological characteristics, present an opportunity for antitumor therapy through the targeted consumption of lactic acid, making it an ideal candidate for lactate depletion in the TME [10,11]. *Rhodospirillum rubrum* (*R. rubrum*) is a typical anaerobic photosynthetic bacterium endowed with a P870 photosystem that consumes small organic acids as electron donors. Under light irradiation, *R. rubrum* efficiently depletes lactate and generates hydrogen by nitrogenase [12,13]. Hydrogen gas (H_2) is a therapeutic medical gas, and because of its inherent biosafety, it is a highly promising strategy against several diseases [14,15]. Therefore, given the lactate consumption and hydrogen production characteristics of *R. rubrum*, we anticipated that it would be suitable for antitumor therapy by remodeling the TME. Unfortunately, natural bioreactions typically are not sufficient to achieve satisfactory therapeutic effects [16,17]. Nanotechnology has made it possible to promote and enrich the function and behavior of microorganism systems at the nanoscale and molecular scales to address current limitations in bioinspired manufacturing. For example, a self-photosensitization approach with CdS nanoparticles for a nonphotosynthetic bacterium has been used for solar-to-chemical production [18]. To enrich the function of detoxification bacteria, concomitant reactive oxygen species (ROS) have been eliminated using cerium oxide nanoparticles (ceria) [19]. To address the lack of controllability in biological materials, nanomaterials are expected to regulate bacterial behaviors. To enrich the function of the microorganism system, material-assisted microorganism-based tumor therapeutic platforms provide a novel means to fight tumors [20]. Small-size gold nanoparticles (Au NPs) have a stable structure and low toxicity as well as high photoelectric converting efficiency [21–23]. Thus, they are ideal photoexcited electron donors and can transfer optical energy to electrons to enhance bacterial metabolic activities. Ultimately, Au NPs can generate hydrogen and deplete lactate with high efficiency and remote controllability.

Inspired by the universal existence of abundant lactate in tumors, the above recognitions have stimulated our interest in the intratumoral bacterial metabolic consumption of lactate and its consequential biological effects against tumors. Herein, we developed a nanogold-engineered *Rhodospirillum rubrum* (R.r-Au) composed of photosynthetic R.r and photoexcited electron donors Au NPs that exhibited the capability of photochemical transformation (Fig. 1). To achieve safe and efficient *in situ* delivery of living bacterial drug, we leveraged a stepwise cryogenic micromolding approach to construct a transdermal therapeutic cryomicroneedle (CryoMN) patch integrated with R.r-Au (CryoMNs-R.r-Au). Through self-metabolism and self-regulation to continuously consume lactate *in situ* and produce hydrogen, the TME system was reshaped and effectively inhibited tumor growth through tumor optical biotherapy. Following laser irradiation, R.r-Au efficiently produced hydrogen and depleted lactate. By down-regulating lactate concentration, the tumor-associated macrophage (TAM) phenotype was directly polarized from an M2 type to an M1 type, restored $CD8^+$ T-cell activity, and inhibited the Treg cells. The results demonstrated R.r-Au's ability to remodel the immunosuppressive TME. Moreover, the CryoMNs-R.r-Au achieved efficient *in situ* delivery of bacterial drugs, significantly improving bioavailability. In keeping with results from long-term storage studies, the viability of R.r-Au in CryoMNs remained

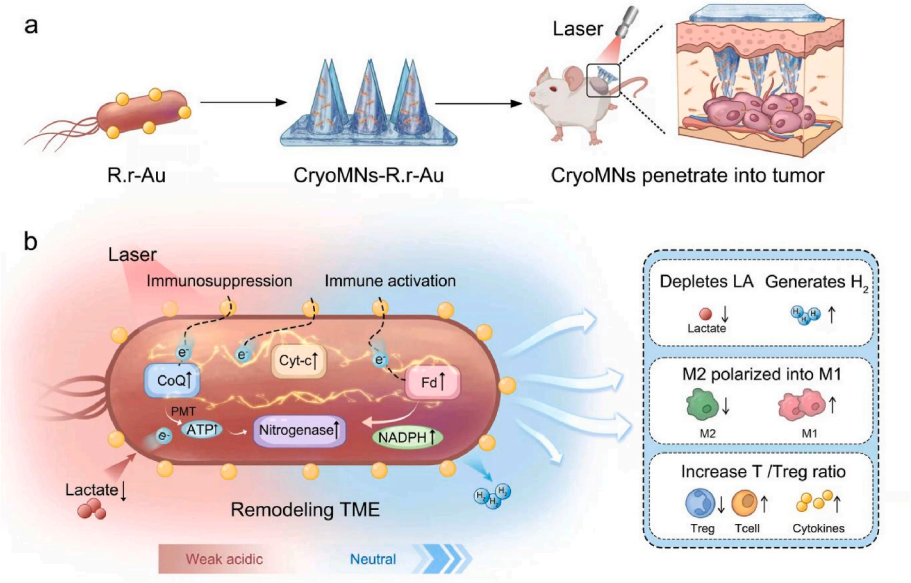

Fig. 1. Schematic outline of the fabrication and application of CryoMNs-R.r-Au. (a) CryoMNs-R.r-Au employing cryomicroneedles for transdermal delivery of nanogold-engineered *Rhodospirillum rubrum* through optical biotherapy for remodeling the tumor microenvironment. (b) Under laser irradiation, R.r-Au can effectively enhance lactate consumption and hydrogen production by photochemical transform through electron transfer into the photosynthetic system of *R. rubrum*, leading to an improved antitumor immune activation.

above 90%. We minimally invasively inserted the CryoMNs into mouse skin, which rapidly dissolved after the deployment of bacterial drugs. No by-products were produced. This combination of optical biotherapy and CryoMNs has facilitated minimally invasive *in situ* delivery of living bacterial drugs and opened up new avenues for nanoengineering bacteria to recycle tumor metabolite into effective substances for tumor optical biotherapy. These findings provide a promising strategy for clinical cancer treatment.

2. Results and discussion

2.1. Construction and characterization of R.r-Au

Au NPs have exhibited excellent biocompatibility, rendering them a superior platform for the fabrication of inorganic-biohybrid systems [24]. First, Au NPs were fabricated according to the citrate-reduction method and attached the Au NPs onto the surface of *R. rubrum* using an Au-S bond [25]. Morphological characterization was accomplished by transmission electron microscopy (TEM; Fig. 2a; Fig. S1, Supporting Information) and indicated that R.r-Au had uniform Au NPs with good monodispersity (diameter about 15 nm). According to the TEM-assisted element mapping images, morphological changes did not occur on the bacteria, and the Au NPs were distributed in a uniform fashion on the cytomembrane of bacteria (Fig. 2b). Because of the efficient attachment of Au NPs (approximately 15 nm) to the surface of *R. rubrum*, the hydrodynamic sizes of R.r-Au were slightly larger than the *R. rubrum*, as shown in the dynamic light scattering measurements (Fig. 2c). The results showed that the sizes of R.r-Au and R.r were in the range of 2–3 μm, which was consistent with the TEM results. The Au NPs were loaded on the surface of *R. rubrum*, and then the R.r-Au displayed a distinct absorption peak at 542 nm. This result was consistent with the characteristic absorption of Au NPs (Fig. 2d; Fig. S2, Supporting Information), and X-ray photoelectron spectroscopy (XPS) was used to identified an Au element on the bacterial cells of R.r-Au, which had characteristic binding energies at 83.4 and 87.7 eV, aligning well with that of Au (0) (Fig. 2e) [26]. We optimized the ratio of Au NPs and R.r in our pre-experiment by hydrogen production efficiency and monitored the retention time of Au NPs on bacteria (Figure S3, S4 and S5). To investigate whether AuNPs conjugation affected the viability of *R. rubrum,* we used SYTO 9 to stain the live *R. rubrum* green. The results showed that Au NPs conjugation with *R. rubrum* did not affect the viability of *R. rubrum* (Fig. 2f). To verify the safety of Au NPs, we cultured *R. rubrum* and R.r-Au with equal amounts of *R. rubrum* at 10 × dilution on solid Luria broth (LB) agar for 24 h. After three trials, we counted the bacterial colonies and observed bacterial growth. According to the results, the number of bacteria colonies formed by *R. rubrum* and R.r-Au were nearly

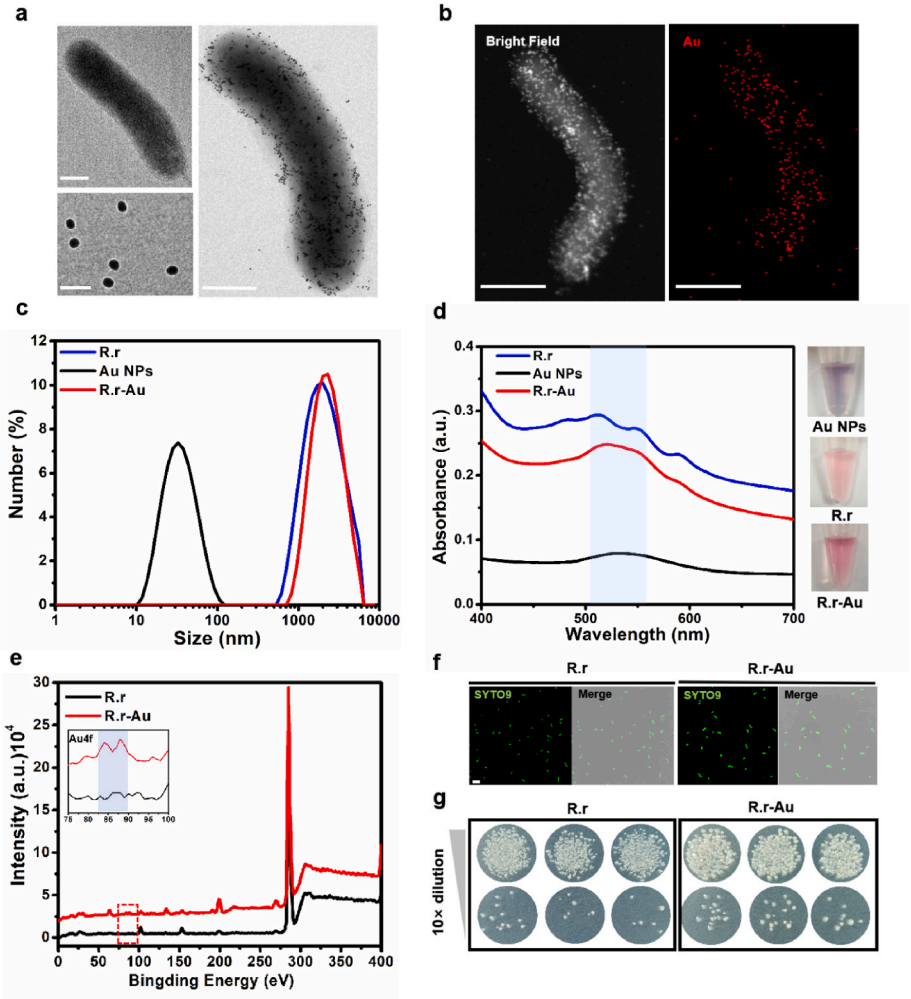

Fig. 2. Characterization of nanogold-engineering *Rhodospirillum rubrum* (R.r-Au). (a) Representative TEM images of Au NPs (left bottom, scale bar = 30 nm), R.r (left, scale bar = 500 nm), and R.r-Au (right, scale bar = 500 nm). Au NPs were attached to the R.r surface as a result of the interaction between the carboxyl and sulfhydryl groups. (b) EDS elemental mapping of Au on R.r surface (scale bar = 500 nm). (c) Hydrodynamic diameter distributions of R.r, Au NPs and R.r-Au. (d) UV–vis absorption spectra of R.r, Au NPs, and R.r-Au. (e) Dried R.r and R.r-Au XPS spectra and Au 4f XPS spectrum of R.r-Au. (f) FL microscopic images of R.r-Au. Live R.r was stained green with SYTO 9 (scale bar = 2 μm). (g) Growth of R.r and R.r-Au was evaluated on solid LB agar. Data are given as mean ± SD (n = 3).

the same. These findings demonstrated that Au NPs and the conjugation process were safe for *R. rubrum* (Fig. 2g).

2.2. AuNPs accelerating photochemical transformation of R. rubrum

We next evaluated the photoelectronic converting property of Au NPs on the bacterial surface. We found that a transient photocurrent response emerged, reaching 0.04 nA under laser irradiation after 40 s (Fig. 3a). This result demonstrated the attractive photoelectronic converting efficiency of R.r-Au, which showed a onefold increase over *R. rubrum*. Six-cycle experiments were conducted and demonstrated that the R.r-Au maintained a steady current intensity. This result showed that R.r-Au could reproduce a photocurrent response while also continuously transferring optical energy to electrons. Thus, we verified that Au NPs could act as photoexcited electron donors to achieve highly efficient photoelectric conversion under laser irradiation. Photosynthetic bacteria have complicated and distinct electron transfer pathways—for example, electron transport proteins are involved in electron transfer. Several membrane-bound proteins are involved in the photosynthetic electron transport (PET) chain, such as coenzyme Q, cytochrome *c*

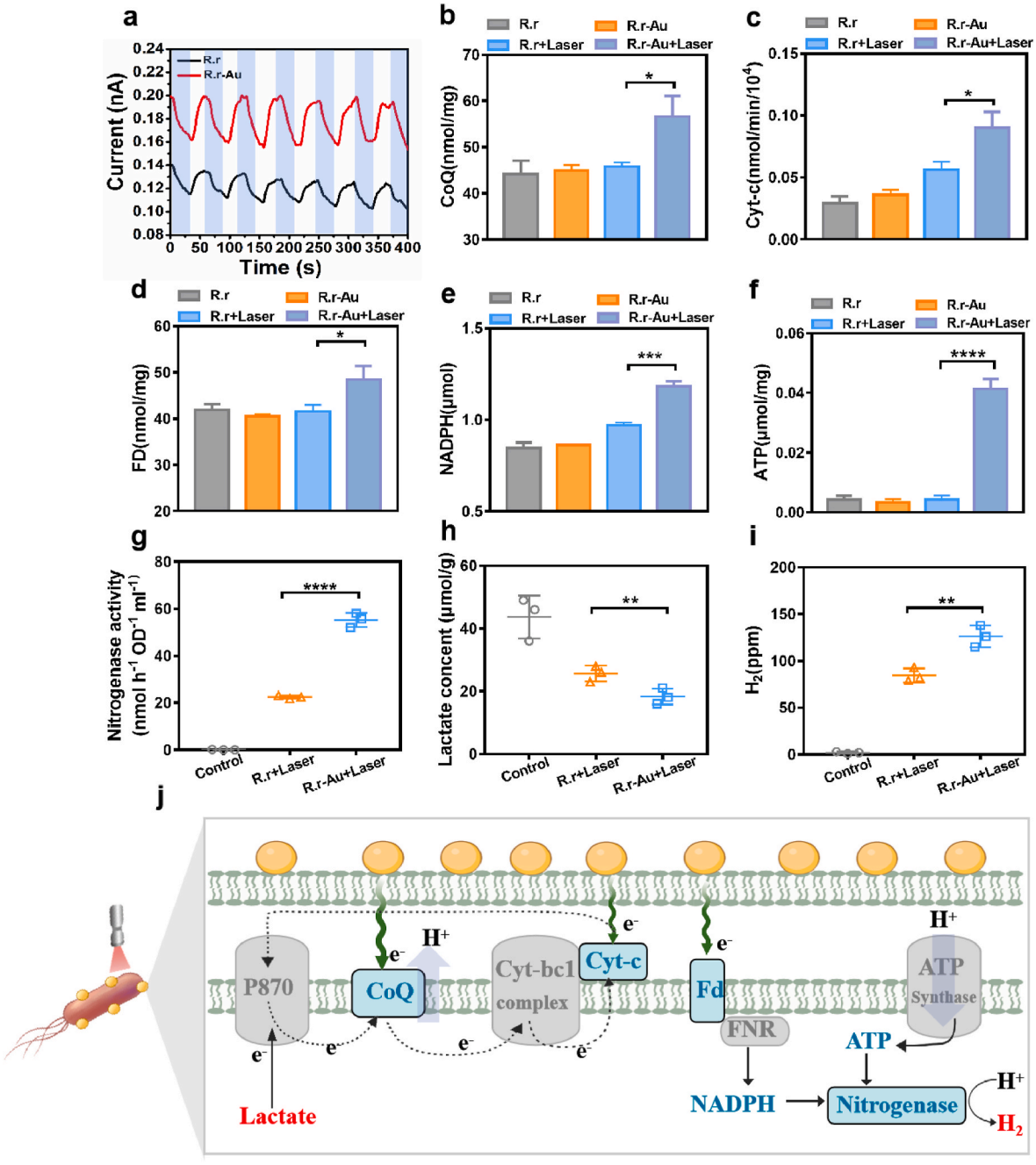

Fig. 3. AuNPs enhance lactate depletion and H_2 production of *Rhodospirillum rubrum* (R.r). (a) Transient photocurrent responses of *R. rubrum* and R.r-Au. We conducted laser irradiation (808 nm, 0.5 W cm^{-2}) at 40, 100, 160, 220, and 280 s. (b)–(f) Intracellular CoQ, Cyt-c, FD, NADPH, and ATP levels of *R. rubrum* and R.r-Au with and without laser irradiation at an equivalent concentration of 109 CFU/mL R.r (808 nm, 0.5 W cm^{-2}, 30 min). (g) After laser irradiation, we measured nitrogenase activity by acetylene/ethylene assay in the headspace (808 nm, 0.5 W cm^{-2}, 30 min). (h)–(i). NIR-photocatalytic lactate consumption and H_2 production behavior of the *R. rubrum* and R.r-Au in N-deficient medium using 40 mM lactate under 808 nm laser irradiation (0.5 W cm^{-2}, 30 min). (j) Schematic illustration of Au NPs promoting *R. rubrum* electron transport and enhancing the metabolic activity of lactate consumption to produce hydrogen. Data are given as the mean ± SD (n = 3).

oxida, ferredoxin, and NAD(P)H-dehydrogenase. All of these proteins receive and transport electrons from photosynthetic and respiratory chains [27–29].

We next explored the metabolic activities of exogenous electrons after they were transferred to bacterial cells. We tested the content of coenzyme Q, cytochrome *c* oxida, ferredoxin, and NAD(P)H-dehydrogenase in bacterial cells. These typical carriers of intracellular electrons determine the metabolic activity of bacterial cells [30–32]. As shown in Fig. 3b–e, the content of coenzyme Q, cytochrome *c* oxidase (Cyt-c), ferredoxin, and NAD(P)H-dehydrogenase of R.r-Au was significantly increased under near-infrared (NIR) laser irradiation, which caused the ATP level to increase by enhancing the proton motive force (Fig. 3f). As a result of the increased content, the photoexcited electrons generated by the Au NPs were transferred effectively to the bacterial cells and boosted the intracellular metabolism of matter and energy. Note that we observed a certain enhancement in Cyt *c* and NADPH from untreated *R. rubrum* under laser, which suggested that the Cyt *c*/NADPH improvement in the laser-irradiated R.r-Au group was partially influenced by the photosynthetic system.

Nitrogenase is a pivotal enzyme in the production of hydrogen (H_2) by *R. rubrum*. To determine nitrogenase activity, we employed an acetylene reduction assay [33]. As shown in Fig. 3g, the nitrogenase activity of R.r-Au exhibited a threefold increase in nitrogenase activity compared with *R. rubrum*. After we demonstrated the transfer process of the material-cell electron under NIR laser irradiation (0.5 W cm^{-2}, 30 min), we assessed the ability of R.r-Au to consume lactate and produce hydrogen. We used an N-deficient medium (MMG, Formulation shown in Table S1) with lactate (40 mM) as the organic carbon source and measured the lactate concentration in the supernatants. In the control group, we found that the lactate concentration did not change and was maintained at 40 mM. In *R. rubrum* and R.r-Au treatments, however, we found that the lactate concentrations decreased to approximately 26 mM and 18 mM, respectively (Fig. 3h). Notably, R.r-Au exhibited a superior capacity for lactate consumption compared with *R. rubrum* at a rate of 1.5-fold. The H_2 content also was tested using gas chromatography (GC). In the *R. rubrum* and R.r-Au groups, the detected content of H_2 evolution was about 82 ppm and 128 ppm, respectively (Fig. 3i). R.r-Au exhibited a superior capacity for hydrogen production compared with *R. rubrum* at a rate of 1.6-fold. The results demonstrated that the photoelectrons generated by Au NPs on the bacterial surface were transferred to the bacterial cytoplasm and experienced accelerated cell metabolism.

The P870 photosystem of *R. rubrum*, a typical anaerobic photosynthetic bacterium, can utilize external lactate as an electron donor to transfer electrons to the photosynthetic system and promote metabolic activities [34]. The results demonstrated that photoelectrons generated by Au NPs on the bacterial surface directly affected CoQ, Fd and Cyt *c* and enhanced CoQ expression levels, thereby promoting cyclic electron transport, enhancing proton motive force, and accelerating ATP synthesis for energy production. In addition, the increased expression of Fd indirectly affected NADPH levels, which in conjunction with ATP, promoted nitrogenase activity for hydrogen production in *R. rubrum* (Fig. 3j).

2.3. Preparation and characterization of CryoMNs-R.r-Au

We increased the distribution of the drug in deeper tumor sites and reduced leakage of therapeutic drugs into adjacent tissues through the transdermal delivery of the R.r-Au and improving the therapeutic effect. When the bacteria were presuspended in a suitable cryoprotectant medium, they were preserved in a cryogenic environment with minimal loss of viability. To efficiently deliver living bacterial drugs, we leveraged a cryogenic micromolding approach to construct a transdermal therapeutic CryoMNs patch integrated with R.r-Au. We presuspended bacteria in the optimized cryogenic medium (5% glycerol in phosphate-buffered saline (PBS)) and cast the obtained mixture into a negative polydimethylsiloxane (PDMS) mold. The PDMS mold included a 16 × 16 MN array; it was 1 mm high and 350 μm wide around each MN. The CryoMN formulation included 5% glycerol and R.r-Au at a concentration of 1×10^9 CFU mL^{-1}. After we loaded the solution into the PDMS mold, we formed low-speed centrifugation at 2000 rpm to load the bacteria into the tip cavities. We peeled off the CryoMNs from the PDMS mold after freezing. The results showed that the conical structure and sharpness of the needles were well replicated (Fig. 4a) [35,36]. The self-fluorescence characteristic of bacteria was advantageous (Ex = 750 nm, Em = 773 nm), and after immersion in cold PBS, the MN tips detached from the base. As shown in Fig. 4b, we observed the red R.r-Au inside the needle.

Mechanical strength is a key parameter of skin penetration. To examine the mechanical strength of CryoMNs with 0–5% glycerol concentrations, we used a tensile testing machine. The CryoMNs handled a load force of 0.2–0.3 N per needle and did not fracture. As shown in Fig. 4c and **d**, a higher glycerol concentration contributed to lower mechanical strength; however, CryoMNs with 5% glycerol maintained sufficient strength and could penetrate the skin (≈0.058 N per needle) [37]. FL microscopic images of R.r-Au. Live R.r was stained green with SYTO 9. We then examined the effect of different glycerol concentrations on bacterial activity by means of live bacteria stained by SYTO 9. As shown in Fig. 4e and Fig. S6, the activity of R.r-Au with different proportions of glycerol were significantly higher than that of control group. Fourteen days after fabrication, we further tested the viability of R.r-Au inside CryoMNs. After 14 days and without any glycerol (0%) in the formulation, the viability of R.r-Au was reduced to less than 50% (Fig. 4f). Added glycerol (1–5%) significantly enhanced the viability to 70–90%. For subsequent tests, we used CryoMNs with 5% glycerol.

Ice usually melts in a typical operating environment at room temperature (RT). The mechanical strength of CryoMNs determines the ability to penetrate the skin and is affected negatively by melting. We used mouse skin to investigate the correlation between skin penetration ability and residence time at RT. Prolonged exposure of CryoMNs to RT resulted in decreased skin penetration ability, with complete loss observed after 50 s (Fig. 4g–h). After 40 s, CryoMNs could penetrate the 50 μm thick stratum corneum. CryoMNs were incubated at RT for less than 30 s and reached the dermal layer up to 300 ± 50 μm deep [38]. CryoMNs should be administered immediately after they are removed from storage, and they should not be exposed to RT for more than 40 s. These results verified that this duration supported the use of CryoMNs to successfully penetrate the skin.

To confirm the safety of this method, we inserted CryoMNs into mice skin using a thumb press. We clearly and immediately saw microholes upon the removal of the needle. Pseudo-colour was added to the skin damage site to facilitate semi-quantitative statistics by the software. Statistical graphs significantly showed the extent of skin damage. As shown in Fig. 4i, the CryoMNs prepared by 0% glycerol concentration caused obvious skin damage 24 h later. With an increase in the glycerin concentration, skin damage gradually decreased, and the administration skin was barely damaged by CryoMNs with 5% glycerol.

2.4. Lactate depletion and hydrogen generation in situ of R.r-Au

Various types of bacteria display distinct taxis behaviors, enabling them to migrate to different areas of the body. However, this can potentially pose a risk of bacterial infection [39]. Therefore, safe and effective methods are needed for *in situ* delivery of bacteria. We used B16F10 tumor-bearing Balb/c mice model to evaluate the *in vivo* biodistribution of *R. rubrum* and R.r-Au after microneedle administration. We collected tumors and major organs. We counted the bacterial colonies in the tissue of these *R. rubrum* and R.r-Au (Fig. 5a and Fig. S7) and found that the *R. rubrum* and R.r-Au colonies (normalized by weight; CFU/g^{-1}) in the tumors were higher than that in other organs on the first day and remained almost unchanged on the third day (Fig. 5b). *R. rubrum* and R.r-Au delivered via CryoMNs achieved excellent retention and accumulation in the tumor site. These results demonstrated that

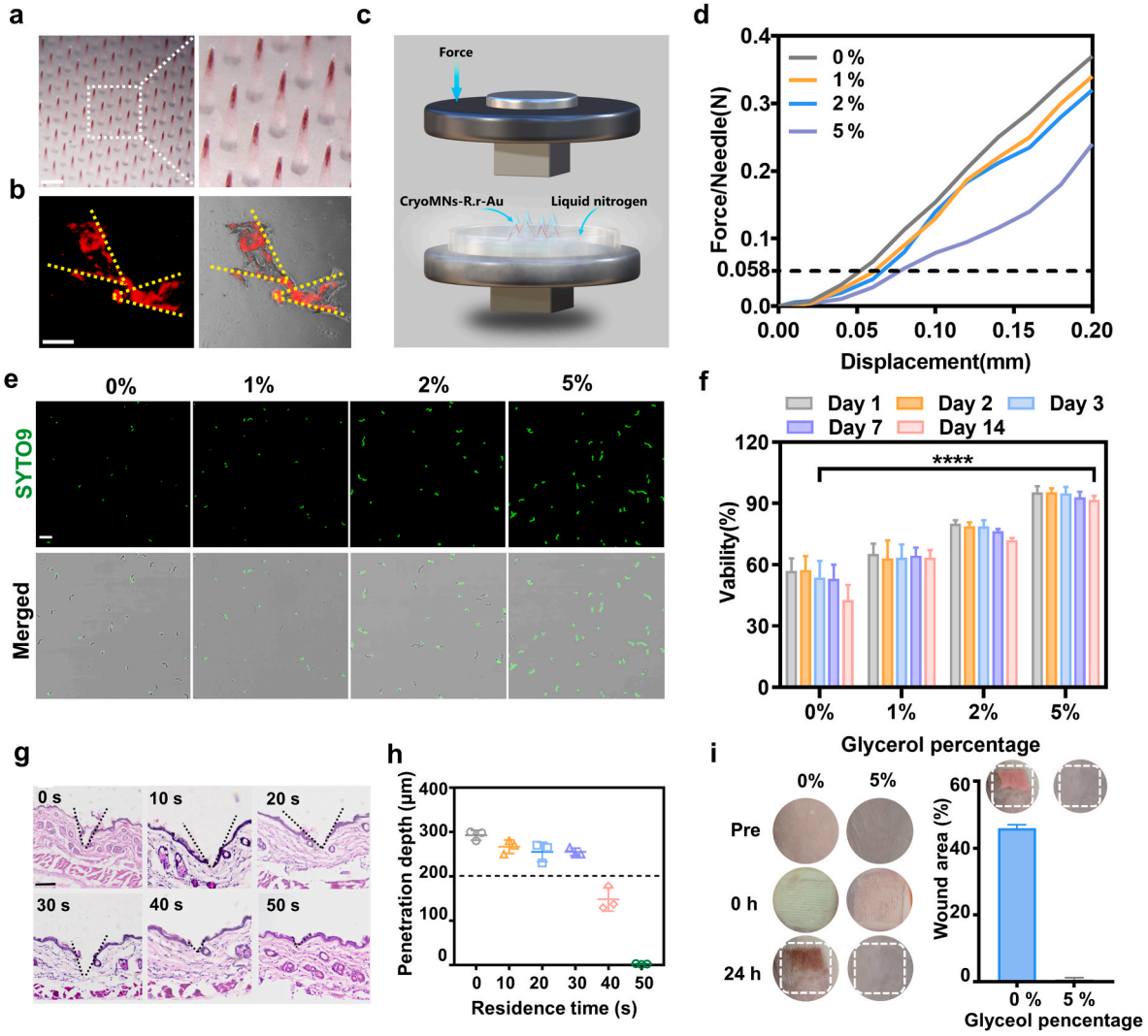

Fig. 4. Preparation of CryoMNs for R.r-Au loading and R.r-Au viability maintenance. (a) CryoMNs-R.r-Au morphology. The CryoMNs-R.r-Au were prepared using the micromolding method and observed by digital microscopy imaging (scale bar = 1 mm). (b) Representative FL images of the individual CryoMNs loaded with R.r-Au (Ex = 750 nm, Em = 773 nm) (scale bar = 200 nm). (c) The loading force of CryoMNs-R.r-Au, which was measured under the protection of liquid nitrogen. (d) CryoMNs-R.r-Au loading force-displacement profiles with different concentrations of glycerol. (e)–(f) Viability of R.r-Au cryopreserved in CryoMNs with different concentrations of glycerol (n = 5). (g) H&E staining of mouse skin. We applied the CryoMNs-R.r-Au patch for 0, 10, 20, 30, 40, and 50 s (scale bar = 100 μm). (h) Corresponding quantitative analysis of skin penetration depth realized by CryoMNs (n = 3). (i) Photographs of skin damage and statistics of skin lesion area in mice 24 h after CryoMNs treatment.

CryoMNs were superior in the delivery of active bacterial drugs. Simultaneously, it was showed that no bacteria were found in either the tumour or the organs on day four. Residual live bacteria were phagocytosed and eventually cleared by host neutrophils and macrophages approximately four days after treatment, which is consistent with literature reports [40].

We demonstrated in vitro that *R. rubrum* efficiently depleted lactate and produced hydrogen under laser irradiation and was a promising means to modulate the TME and kill tumor cell for tumor growth inhibition. We next investigated whether R.r-Au could be used for *in vivo* antitumor therapy and assessed the ability of R.r-Au to deplete lactate and produce hydrogen in a tumor. Because gas bubbles offered a strong contrast under ultrasonic imaging, we used this imaging to monitor hydrogen gas generation in the tumor. We administered CryoMNs-R.r-Au to the tumor under laser irradiation (808 nm, 0.5 W cm^{-2}, 30 min) and identified ultrasound signals in the tumor, which demonstrated that gas production was efficient. Consistent with the results of in vitro, R.r-Au showed better hydrogen generation. The R.r-Au group exhibited a twofold increase in hydrogen signal intensity compared with the *R. rubrum* group under identical laser irradiation conditions (Fig. 5c and d).

We next monitored the intratumoral pH value on mice with B16F10 tumors using a pH-sensitive fluorescent probe (BCECF) with multispectral fluorescence imaging [41]. An acidic intratissue pH appeared on the control tumors at 6.0–6.5, and the CryoMNs-R.r (+) and CryoMNs-R.r-Au (+) group tumors displayed a pH value close to neutral or neutral (Fig. 5e and **f**). In addition, the pH level of CryoMNs-R.r-Au (+) treatment group was higher than that of the CryoMNs-R.r (+) treatment group. This result indicated that bacteria could change the pH value in the tumor by sustainably depleting lactic acid, which changes the acidic immunosuppressive TME.

2.5. Optical biotherapy and immune activation of R.r-Au in vivo

We constructed a subcutaneous mouse B16F10 tumor model to study the potential of R.r-Au to inhibit tumor progression. We subcutaneously injected Balb/c mice with 1×10^8 B16F10 cells. On the fourth day, we divided the tumor-bearing mice into five random groups (n = 5 per

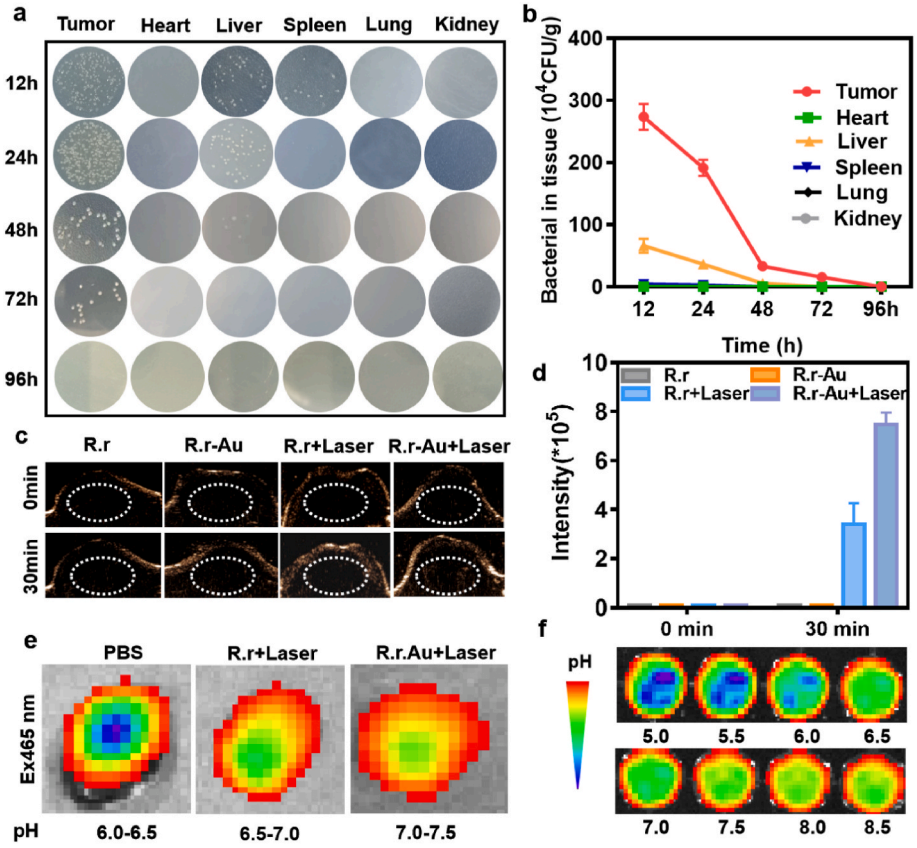

Fig. 5. Transdermal delivery of R.r-Au via CryoMNs for intratumoral lactate depletion and hydrogen generation. (a) Biodistribution of R.r-Au *in vivo*. Homogenates of tumor and major organs were collected and cultured on solid LB agar for bacterial colony observation. (b) We quantitatively measured R.r-Au distribution in different tissues at different time points. (c) Ultrasound images that monitored the hydrogen-generating level of the R.r-Au in the tumor region under NIR irradiation by laser (808 nm, 0.5 W cm^{-2}, 30 min). (d) Corresponding quantitation of ultrasound signal intensities appeared in the tumor region after laser irradiation. (e) Multispectral fluorescence images indicated intratumoral lactate depletion and tumor pH change. We used a BCECF for pH value visualization (λex = 465 nm). (f) The BCECF fluorescence signal in PBS had different pH values.

group), as follows: PBS, CryoMNs-R.r, CryoMNs-R.r-Au, CryoMNs-R.r (+), and CryoMNs-R.r-Au (+). In the CryoMNs-R.r (+) and CryoMNs-R.r-Au (+) group, we first administered CryoMNs and then laser irradiation for 30 min (808 nm, 0.5 W cm^{-2}). Each mouse received the same administration every two days for a total of three doses (Fig. 6a). We verified the antitumor effect by measuring the volume growth, weight, and image of harvested tumors (Fig. 6b–d). B16F10 tumors in the CryoMNs-R.r and CryoMNs-R.r-Au without exposure to the laser irradiation treatment group grew rapidly, which was consistent with the PBS group. We observed more significant tumor inhibition in the laser-treated group than in the group without irradiation. This result indicated that higher antitumor activity was attributed mainly to the laser, which effectively promoted the metabolic activity of bacteria to deplete lactate and generate hydrogen. In particular, Studies have shown that the expression of intratumoral vascular endothelial growth factor may be suppressed by an excessive number of hydrogen molecules and may initiate a systematic immunoreaction [42,43]. Furthermore, in CryoMNs-R.r-Au (+) treatment group had a stronger antitumor effect because the Au NPs on the surface of the bacteria could further promote the metabolic activity of the bacteria. We waited 14 days after tumor inoculation to record mouse survival. As expected, because of the efficient antitumor effect, the CryoMNs-R.r (+) and CryoMNs-R.r-Au (+) treatments had the highest survival rates (Fig. S8).

Tumor-derived lactate inhibited the activity of $CD8^+$ T cells and affected the polarization of the TAM phenotype because of glycolysis in tumor cells, which is the key regulator of the immunosuppressive TME. Therefore, we tested the tumor lactate concentration after different treatments. We detected a lower level of lactate in the CryoMNs-R.r-Au (+) treatment group than in the control groups. This result demonstrated that significant tumor growth was inhibited in the CryoMNs-R.r-Au (+) treatment group, which was due to the reduced levels of lactate at the tumor site (Fig. 6e).

To better understand the influence of this combined therapy, we also investigated changes in the TME after lactate depletion and hydrogen generation. We evaluated the immune responses in tumor tissues after the different treatments and detected typical types of cells that had innate immunity (macrophages) and cellular immunity (T cells). After various treatments, we killed the mice with the B16F10 tumors and used a flow cytometry (FCM) assay to detect the macrophages' phenotype in the tumor tissues. The number of macrophages in the treated group without laser irradiation (CryoMNs-R. r and CryoMNs-R.r-Au) was not significantly different from the PBS group. CryoMNs-R. r (+) with laser radiation showed slight changes. The CryoMNs-R.r-Au (+) group, however, had a significantly lower percentage of M2-type TAMs (the $CD206^+F4/80^+$cells were 5%). The competency of the M1-type TAMs also increased (the $CD86^+F4/80^+$ cells were 21%) (Fig. 6f). The effective lactate depletion ability of CryoMNs-R.r-Au (+) was attributed to the ability of lactate to induce differentiation in M2 macrophages. We also used fluorescence-activated cell sorting (FACS) to detect the proportion of activated T cells (IFN-γ^+ CD8) (Fig. 6g and S9,S10f). We found an increased proportion of IFN-γ^+ CD8 T cells in the CryoMNs-R.r-Au (+) group, which demonstrated that the activation ability of the CryoMNs-R.r-Au (+) treatment group was good for cellular immunity.

We conducted a quantitative analysis, and the results showed that the IFN-γ^+ CD8 T cells in the CryoMNs-R.r-Au (+) group were 3 and 1.8 times higher than those of the PBS and CryoMNs-R.r (+) groups,

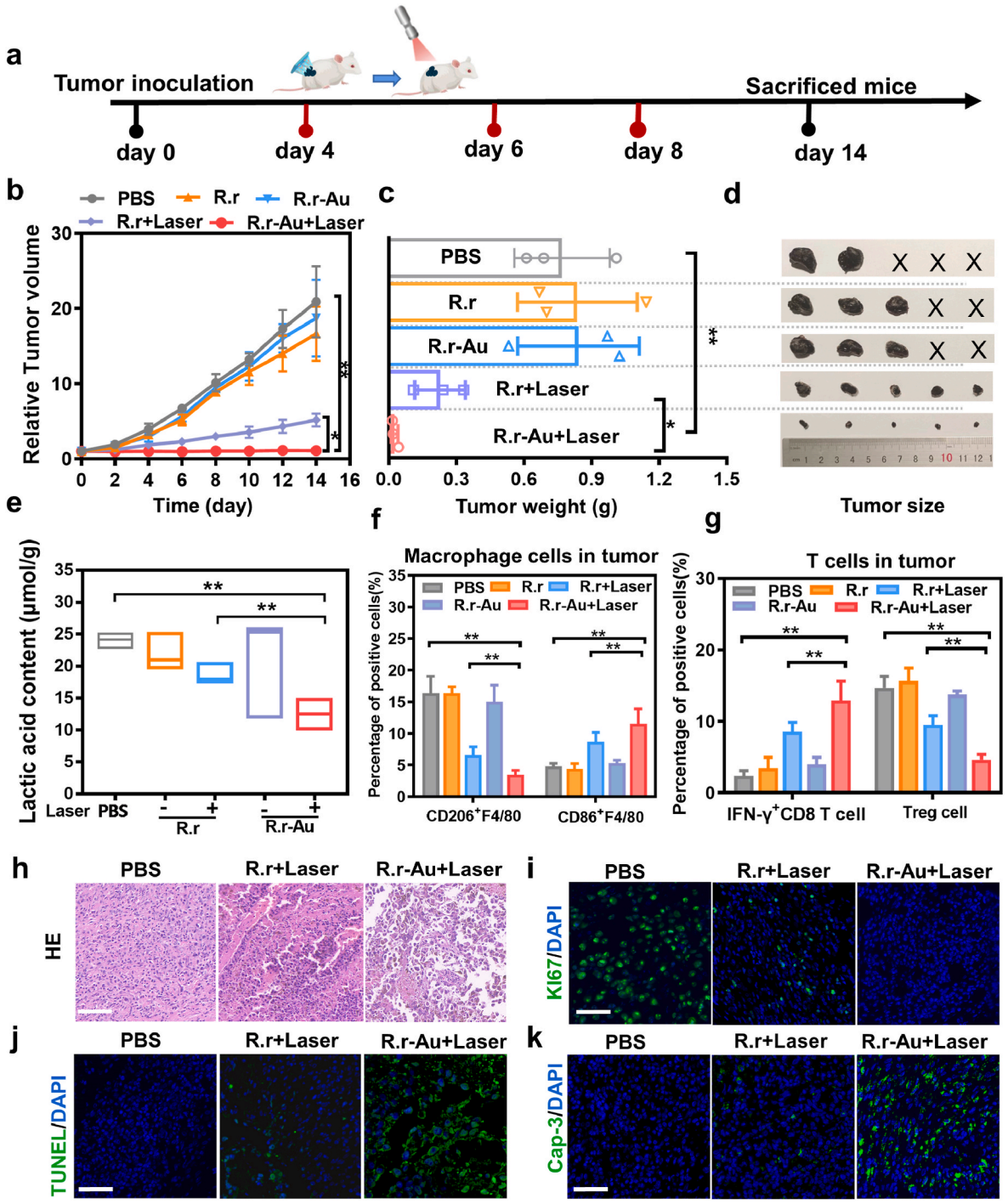

Fig. 6. The CryoMNs-R.r-Au patch inhibits tumor growth by depleting lactate levels and generating hydrogen to remodel the TME. (a) Experimental approach to evaluate the antitumor effect of the CryoMNs-R.r-Au patch. The red line indicates the day of treatment. (b) Relative volume curves of tumor growth in different treatments (n = 5). (c, d) Size and weight of the extracted B16F10 tumors after day 14 (n = 5). (e) Tumor lactate concentration after different treatments. (f) Tumor-associated macrophage cells (TAMs; M2: $CD206^+$ F4/80, M1: $CD86^+$ F4/80) in tumor tissues following FCM analysis. (g) FCM detection of the component of Treg cells and IFN-γ^+ CD8 T cells. (h)–(k) Immunofluorescence staining of tumor histologic sections after different treatments, including H&E staining and Ki67 proliferating cells, $TUNEL^+$ apoptotic cells, and Cap3+ apoptotic cells (scale bar = 50 μm).

respectively. To verify the efficiency of removing the immunosuppressive TME by the CryoMNs-R.r-Au (+) treatment group, we detected the percentage of Treg cells. The FCM results suggested that CryoMNs-R.r-Au (+) markedly decreased the component of Treg cells (the percentage of $FOXP3^+CD4^+CD25^+$ was 5%) (Fig. 6g). To further evaluate the antitumor capability of CryoMNs-R.r-Au (+), we used enzyme-linked immunosorbent assay (ELISA) to analyze the antitumor cytokines in the tumor tissue homogenates. We detected the highest levels of TNF-α and IFN-γ in the CryoMNs-R.r-Au (+) group (Fig. S12). After therapy, the results of H&E staining images showed that the CryoMNs-R. r (+) and CryoMNs-R.r-Au (+) experienced serious damage to tumors, which caused a significant amount of tumor cell death (Fig. 6h). Terminal deoxynucleotidyl transferase-mediated deoxyuridine triphosphate nick end labeling-positive ($TUNEL^+$) and Caspase-3-positive ($Cap3^+$) cellular

apoptosis both increased remarkably (Fig. 6j and **k)**. The $Ki67^+$ tumor cell proliferation was nearly suppressed (Fig. 6i). CryoMNs-R.r (+) and CryoMNs-R.r-Au (+) both exhibited excellent tumor suppression ability, which attributed to the combined therapy of lactate consumption and hydrogen generation.

The results of this study demonstrated that the CryoMNs-R.r-Au (+) group effectively decreased the percentage of Treg cells, polarized the TAMs phenotype from the M2 type to M1 type, and restored $CD8^+$ T-cell activity by generating hydrogen and depleting lactic acid in the TME. We attributed the good outcomes to the fact that the TME was completely altered by R.r-Au-CryoMNs (+) therapy.

To examine the long-term anti-tumour immune effect, we extended the treatment duration to 26 days and performed a comprehensive assessment of the treatment effect (Fig. S10). Unsurprisingly, we observed a more pronounced tumour suppression in the laser-treated group compared to the unirradiated group. The results suggest that the efficient anti-tumour activity was mainly attributed to the laser promoting the metabolic activities of lactic acid consumption and hydrogen production by the bacteria. In particular, the stronger anti-tumour effect in the CryoMNs-R.r-Au (+) treatment group was attributed to the fact that the Au NPs on the bacterial surface further promoted the metabolic activities of the bacteria (Fig. S10 b-d). To further investigate the impact of inhibiting R.r-Au on the immunosuppressive tumor microenvironment (TME) and enhancing the immune response *in vivo*, we conducted a flow cytometry (FCM) assay to assess the presence of immune-promoting cells (CD4 T cells, CD8 T cells, NK cells) within the tumor tissues.The analysis of immune-promoting cells, including CD4 T cells, CD8 T cells, and NK cells, in B16F10 tumor tissues provided further confirmation of the enhanced immune response. The result shows that group treated with CryoMNs-R.r-Au (+) exhibited a significantly higher proportion of these immune cells compared to the other groups. The percentages of CD8 T cells, CD4 T cells, and NK cells were 17.0%, 22.3%, and 11.2%, respectively, in the B16F10 tumor-bearing mice (Fig. S10 e-g). These results strongly support the notion that R.r-Au effectively alleviates the immunosuppressive TME and activates the immune response through the synergistic effects of lactate consumption and hydrogen generation.

Because biosafety is a common concern, we evaluated the safety of this cancer treatment model in mice. The results demonstrated that these treatments did not affect the body weight of mice (Fig. S11). We investigated the toxicity of R.r-Au to major organs by H&E staining, which again showed no histopathological lesions (Fig. S13a). We measured serum aspartate aminotransferase (AST)/alanine aminotransferase (ALT) (liver function), and serum urea nitrogen (UREA)/creatinine (CREA) (renal function) to evaluate liver and kidney function. These biochemical indicators did not have any significant differences among all groups (Figs. S13b–S13d). Hence, we determined that significant inflammation and other toxicity *in vivo* were not caused by R.r-Au-mediated tumor optical biotherapy.

3. Conclusions

We developed the nanogold-engineered Rhodospirillum rubrum (R.r-Au) using CryoMNs for a transdermal bacterial delivery method to achieve safe and high-efficiency tumor optical biotherapy. Under laser irradiation, the Au NPs on the bacterial surface generated a large number of photoelectrons using the PET chain pathway. This resulted in efficient lactate consumption and hydrogen production, and as a result, the TME was effectively remodeled. Overall, the combination of optical biotherapy and CryoMNs allowed for minimally invasive and precise delivery of living bacterial drugs and provided new avenues for nano-engineering bacteria to recycle tumor metabolite into effective substances for tumor optical biotherapy. The results verified that this is a promising strategy for anticancer treatment.

4. Experimental section

4.1. Materials

We purchased chloroauric acid ($HAuCl_4$) from Nanjing Chemical Reagent Co., Ltd. (Jiangsu, China). We purchased Tris-(2-carboxyethyl)-phosphine hydrochloride (TCEP) from Sigma Aldrich Co., Ltd. (St. Louis, MO, USA). We purchased a pH-sensitive fluorescent probe (BCECF, 2,7-bis(2-carboxyethyl)-5-(and-6)-carboxyfluorescein) and an $NADP^+$/NADPH Assay Kit with WST-8 and ATP Assay Kit from Beyotime Biotechnology Co., Ltd. (Beijing, China). We purchased Microorganism Coenzyme Q (CoQ) ELISA Kit, cytochrome C oxidase ELISA Kit and Microorganism Ferroredoxin reductase (FDX) ELISA Kit from Qi Yi Biological Technology Co., Ltd. (Shanghai). We purchased lactate acid and glycerol from Nanjing Chemical Reagent Co., Ltd. We purchased a live/dead bacterial viability kit from Invitrogen Co., Ltd. (Carlsbad, CA, USA). All reagents and chemicals were of analytical grade and did not require further purification. We purchased TNF-α and IFN-γ ELISA kits, Perc/Cyanine5.5-conjugated F4/80 antibody, PE-conjugated CD86 antibody, APC-conjugated CD206 antibody, FITC-conjugated CD3 antibody, APC-conjugated IFN-γ antibody, and Perc/Cyanine5.5-conjugated CD8 antibody, from BioLegend (San Diego, CA, USA).

4.2. Synthesis of Au NPs

Au NPs with a size of about 16 nm were synthesized by the citric acid reduction method. We dissolved 10 mg chloroauric acid ($HAuCl_4$) in 100 mL ultrapure water and heated it to boiling under magnetic agitation. Then, 3 mL 1 wt % sodium citrate aqueous solution was rapidly injected into this solution. We continued to heat the solution for 30 min. When the solution turned red, we obtained the size of 16.0 ± 1.1 nm Au NPs. We then cooled the solution to RT and stored it at 4 °C.

4.3. Fabrication of R.r-Au

We collected bacteria at a density of 10^9 CFU mL^{-1} in 2 mL tubes. We used centrifugation for 5 min at 6000 rpm. We suspended the collected filter in 1 mL of PBS with 1 mM TCEP, which was incubated for 20 min at 30 °C. We washed the bacteria twice with PBS twice after incubation. Then we conjugated the bacteria with 1 mL Au NPs solution. To create a coupling reaction, we gently agitated the mixture for 2 h at 30 °C. We separate the R.r-Au from the unbound nanoparticles by centrifugation at 6000 rpm and then rinsed the Au NPs with PBS three times.

4.4. Characterization

We obtained the TEM images using a transmission electron microscope (Tecnai G2 F20 S-Twin, USA). XRD analysis was performed with a Oxford Xplore 30 X-ray diffractometer. The size distribution of the R.r, Au NPs and R.r-Au was measured by a Zetasizer Nano (Malvern MS Micro, U.K.).We measured the UV–vis absorbance using UV–vis spectroscopy (PerkinElmer Lambda25, USA). XPS was recorded with a Thermo Scientific Nexsa XPS multi-technique surface analysis instrument. Loading efficiency of gold nanoparticles on bacterial surface was detected by ICP-MS (Agilent 7700 ICPMS, USA). Live/dead bacterial viability assay was carried out by Confocal laser Scanning microscope (Leica TCS SP5, USA).

4.5. Electrochemical measurement

We studied the photocurrent of R.r-Au using an electrochemical analysis system (VersaSTAT 3,USA) with a standard three-electrode system composed of a platinum electrode, a saturated calomel electrode (SCE), and a modified glassy carbon electrode (GCE) (3 mm in diameter). The modified GCE working electrode was prepared with a coating carbon cloth. A piece of acid-treated (H_2SO_4/HNO_3, 3:1) carbon

cloth (1 × 1 cm, projected area cm^2) was placed into a PE tube and soaked with the R.r-Au suspension (10^9 CFU mL^{-1}), which was dispersed in PBS solution, and then stored at 4 °C for 24 h to make a firm attachment of R.r-Au and carbon cloth. The 0.1 M Na_2SO_4 solution was used as the electrolyte. An 808 nm laser was used as the light source. We repeated R.r following the same operation as the control.

4.6. Photoelectrons transfer efficiency

We detected NADPH content using an NADP+/NADPH Assay Kit with WST-8. The collected R.r-Au (10^9 CFU mL^{-1}) were resuspended in MMN containing 40 mM lactic acid solution and irradiated by an 808 nm laser for 30 min. After the irradiation, we harvested R.r-Au by centrifuging (600 g, 5 min). We added a lysis buffer to promote cell lysis. Then, we performed centrifugation at 12,000*g* for 10 min, and the supernatant was taken as the sample for testing. ATP, CoQ, Fd, and Cyt-c were measured using the same experimental conditions as NADPH. Following a 30 min laser irradiation at 808 nm, the measurements were performed following the manufacturer's protocol.

4.7. Lactate detection and generated H_2

To demonstrate that bacteria can produce hydrogen by consuming lactate, we resuspended R.r-AuNPs (10^9 CFU mL^{-1}) in MMG containing 40 mM lactic acid solution, and let it stand in the dark for 3 h at 30 °C. Then, it was irradiated for 30 min with an 808 nm laser. We detected the lactate content with a lactate assay kit following the manufacturer's protocols. We detected the H2 evolution in the 30 mL gaseous phase of the parallel vials by GC (GC9790II) using the TCD mode and then quantified the results using standard curves.

4.8. Fabrication of CryoMNs-R.r-Au

We obtained the PDMS mold from Anhui Zhongding Yuxuan New Material Technology Co., Ltd. (China). The tip was 1000 μm high and the base was 300 μm wide. First, we introduced 400 μL of bacteria suspension (10^9 CFU mL^{-1}) into the mold. We subjected the PDMS mold to centrifugation for 5 min at 2000 rpm, which facilitated the infusion of the solution into the needle cavities. We extracted the excess medium from the base of the mold and introduced a fresh cryogenic medium to fill it. Subsequently, we subjected the PDMS mold to −20 °C for 4 h. We carefully detached the CryoMNs from the PDMS mold and following by freezing at −80 °C for 2 h and at −196 °C (in liquid nitrogen) for 1 h.

4.9. Mechanical strength test of CryoMNs

We examined the mechanical strength of the CryoMNs using a tensile strength tester (ETM501B, China). We maintained the test environment at low-temperature conditions with the continuous addition of liquid nitrogen. We placed the CryoMNs on a flat stainless-steel plate with the tips facing upward and then applied vertical force to the tips at a constant speed of 0.5 mm s^{-1}. When the needle began to bend, we recorded the destructive force of the CryoMNs.

4.10. Viability assay of R.r-Au

We assessed the viability of CryoMNs-R.r-Au using a live/dead backlight bacterial viability kit following the manufacturer's protocol. We used green FL SYTO9 dye to detect viable R.r-Au and placed the stained bacteria in an eight-well chamber for 30 min at 37 °C. Then we used a confocal laser scanning microscope (Leica TCS SP5, USA) to analyze the results.

4.11. Skin penetration ability of CryoMNs

We removed CryoMNs-R.r-Au from liquid nitrogen and stored it at RT (24 °C) for 0, 10, 20, 30, 40, and 50 s. We delivered the CryoMNs-R.r-Au into mice skin using transdermal thumb pressure, which was followed by fixation with 4% paraformaldehyde, tissue sectioning, and H&E staining. We analyzed the depth of penetration of CryoMNs-R.r-Au at different time points at RT using fluorescence microscopy (Olympus CKX53, JPN).

4.12. Biodistribution of R.r-Au in vivo

We used Plate count agar to investigate the bio-distribution of bacteria following in-situ drug delivery from cryomicroneedles. At 12, 24, 48, and 72 h after the administration of thecryomicroneedles, the tumor and other tissue organs were subjected to sterile grinding. Subsequently, the resulting homogenate was centrifuged at 1500 rpm for 5 min to collect the bacteria-containing supernatant. This supernatant was then diluted 10^4 times and carefully dropped onto LB agar plates. Subsequently, the plates were placed in an incubator at 30 °C for a 24 h period to allow for bacterial growth.

4.13. Measurement of H_2 generation in vivo

We inserted the CryoMNs-R.r-Au into mice with B16F10 tumors, and used microneedle melts to release the drug. We used ultrasound imaging (Vevo (TM)2100, Canada) to verify hydrogen production in tumors after laser irradiation at different times.

4.14. Measurement of intratumoral pH variation

We used a pH-sensitive fluorescent probe (BCECF) for the pH imaging. We i.t. Injected the B16F10 tumor-bearing mice with BCECF (0.5 mM), and then killed the mice after 30 min. We immediately harvested the tumor tissue and imaged the sample with the Small animal imaging system (Maestro, USA).

4.15. Animals and tumor model

We purchased female BALB/c mice (5–6 weeks) from Zhejiang Vital River Laboratory Animal Technology Co., Ltd. (Beijing, China). The Institutional Animal Care and Use Committee (IACUC) at Shenzhen Institutes of Advanced Technology, Chinese Academy of Sciences (IACUCN umber, SIAT-IACUC-20210317-YYS-NMZX-TXF-A1712-01) approved this use. We established the melanoma cancer models by suspending the B16F10 cells (1 × 10^7/mL) in PBS, which were then inoculated into the flank of the BALB/c mice. We measured tumor volume using vernier calipers, which was calculated as follows: tumor volume = length × $(width)^2/2$. The maximum tumor burden in mice was 2000 mm^3 in this experiment.

4.16. Optical biotherapy of CryoMNs-R.r-Au in vivo

We distributed the mice into five random groups after the tumor volume reached 150–200 mm^3: untreated, CryoMNs-R.r, CryoMNs-R.r-Au, CryoMNs-R.r + Laser, and CryoMNs-R.r-Au + Laser. Each group of mice received treatment on days 4, 6, and 8. We applied one patch of CryoMNs to deliver 1 × 10^8 CFU mL^{-1} bacteria to each mouse for each treatment. After administering the CryoMNs, we irradiated the tumors with a laser (808 nm, 0.5 W cm^2) for 30 min. Three hours later, we provided light for 30 min. The laser power density maintained a mild temperature below 37 °C for the CryoMNs-R.r + Laser, and CryoMNs-R.r-Au + Laser groups. After 14 days, we excised lymph nodes, tumor tissues, and major organs (heart, lung, liver, spleen, and kidney) from the mice. We used the end of a sterile syringe to homogenize lymph nodes, tumor tissues, and partial spleen by grinding and then processed a single-cell suspension to conduct the flow analysis.

4.17. Evaluation of immune microenvironment in B16F10 tumor

After administering the treatment to each group of mice, the mice tumor tissues were excised. The tumor tissue was then placed in a 2 mL centrifuge tube to which 1 mL of tumor tissue digestion fluid was added. Subsequently, the tumor tissue was finely minced using scissors, and the digestion process was conducted in a constant temperature chamber at 37°Cfor 2 h. Following digestion, the resulting mixture was passed through a 200-mesh nylon membrane to filter out any solid debris. The filtrate was then centrifuged at 1200 rpm for 5 min to obtain a single-cell suspension and analyzed the killer cytokines released by tumor cells with flow cytometry.

4.18. Biosafety evaluation

The supernatant serum was collected by centrifugation at 3000 rpm for 15 min. Biochemical assay kits (aspartate aminotransferase (AST), creatinine (CRE), alanine aminotransferase (ALT), urea nitrogen (BUN)) were used to evaluate the biosafety of CryoMNs-R.r-Au. The heart, liver, spleen, lung and kidney tissues of mice were collected and fixed with 4% paraformaldehyde for 24 h. The tissues were sliced by paraffin embedding and analyzed by H&E staining, and the safety of organs in the whole body was evaluated.

4.19. Statistical analysis

We analyzed data using one-way analysis of variance (ANOVA) and Student's t-test, which was followed by Tukey's post-test. We expressed results as the mean ± standard error of the mean.

Data availability

The research data cannot be shared at this time due to technical or time limitations.

Ethics approval and consent to participate

The Institutional Animal Care and Use Committee (IACUC) at Shenzhen Institutes of Advanced Technology, Chinese Academy of Sciences (IACUCN umber, SIAT-IACUC-20210317-YYS-NMZX-TXF-A1712-01) approved this use.

CRediT authorship contribution statement

Qingxia Shi: Writing – review & editing, Writing – original draft, Visualization, Software, Project administration, Methodology, Formal analysis, Data curation, Conceptualization. **Ting Yin:** Writing – review & editing, Supervision, Methodology, Formal analysis, Data curation, Conceptualization. **Cuiping Zeng:** Supervision, Methodology, Formal analysis. **Hong Pan:** Visualization, Methodology, Formal analysis, Data curation. **Ze Chen:** Methodology, Formal analysis, Data curation. **Lin Wang:** Software, Methodology, Formal analysis. **Bo Wang:** Writing – review & editing, Supervision, Methodology, Investigation, Formal analysis, Data curation, Conceptualization. **Mingbin Zheng:** Writing – review & editing, Supervision, Methodology, Data curation, Conceptualization. **Lintao Cai:** Writing – review & editing, Visualization, Supervision, Resources, Methodology, Funding acquisition, Data curation, Conceptualization.

Declaration of competing interest

The authors declare no conflict of interest.

Acknowledgements

S., T. Y., C. Z. contributed equally to this work. This work was supported by the National Key Research and Development Program of China (2023YFA0915400, 2022YFC2402400), Guangdong Provincial Key Area R&D Program (2020B1111540001), National Natural Science Foundation of China (82303768, 82302374), Guangdong Province Universities and Colleges Characteristic Innovation (2021KTSCX036), Traditional Chinese Medicine Research Project of Guangdong Province Traditional Chinese Medicine Bureau (20221206), Shenzhen Medical Research Fund (A2303057), the Natural Science Foundation of Guangdong Province (2022A1515010780, 2022A1515011337), the Shenzhen Science and Technology Program (JCYJ20210324101807020, JCYJ20200109114616534), Guangdong Basic and Applied Basic Research Foundation (2022A1515111168), Discipline Construction Project of Guangdong Medical University (4SG24015G) and Funds for PHD researchers of Guangdong Medical University in 2024.

Appendix A. Supplementary data

Supplementary data to this article can be found online at https://doi.org/10.1016/j.bioactmat.2024.03.032.

References

[1] E. Boedtkjer, S. Pedersen, Annu. Rev. Physiol. 82 (2020) 103–126.
[2] P. Apostolova, E. Pearce, Trends Immunol. 43 (2022) 969–977.
[3] M. Certo, C. Tsai, V. Pucino, P. Ho, C. Mauro, Nat. Rev. Immunol. 21 (2021) 151–161.
[4] J. Zhao, Z. Tian, S. Zhao, D. Feng, Z.X. Guo, L. Wen, Y. Zhu, F. Xu, J. Zhu, S. Ma, J. Hu, T. Jiang, Y. Qu, D. Chen, L. Liu, Adv. Sci. 10 (2023).
[5] L. Feng, Z. Dong, D. Tao, Y. Zhang, Z. Liu, Natl. Sci. Rev. 5 (2018) 269–286.
[6] C. Hayes, C. Donohoe, M. Davern, N. Donlon, Cancer Lett. 500 (2021) 75–86.
[7] J. Chen, Y. Zhu, C. Wu, J. Shi, Chem. Soc. Rev. 52 (2023) 973–1000.
[8] J. Gu, J. Sun, Y. Liu, G. Chong, Y. Li, H. Dong, Nano Res. 16 (2023) 654–671.
[9] H. Pan, M. Zheng, A. Ma, L. Liu, L. Cai, Adv Mater 33 (50) (2021) e2100241.
[10] J. Wang, Q. Chen, G. Luo, Z. Han, W. Song, J. Yang, W. Chen, X. Zhang, ACS Nano 15 (2021) 17870–17884.
[11] Q. Chen, J. Wang, X. Wang, J. Fan, X. Liu, B. Li, Z. Han, S. Cheng, X. Zhang, Angew. Chem., Int. Ed. 59 (48) (2020) 21562–21570.
[12] A. Dadak, M. Aghbashlo, M. Tabatabaei, H. Younesi, G. Najafpour, J. Clean. Prod. 139 (2016) 157–166.
[13] H. Gest, M. Kamen, Science 109 (1949) 558–559.
[14] Y. Wu, M. Yuan, J. Song, X. Chen, H. Yang, ACS Nano 13 (2019) 8505–8511.
[15] P. Zhao, Z. Jin, Q. Chen, T. Yang, D. Chen, J. Meng, X. Lu, Z. Gu, Q. He, Nat. Commun. 9 (1) (2018) 4241.
[16] D. Zheng, Y. Chen, Z. Li, L. Xu, C. Li, B. Li, J. Fan, S. Cheng, X. Zhang, Nat. Commun. 9 (1) (2018) 9.
[17] B. Wang, K. Xiao, Z. Jiang, J. Wang, J. Yu, P. Wong, Energy Environ. Sci. 12 (2019) 2185–2191.
[18] K. Sakimoto, A. Wong, P. Yang, Science 351 (2016) 74–77.
[19] P. Pan, J. Fan, X. Wang, J. Wang, D. Zheng, H. Cheng, X. Zhang, Adv. Sci. 6 (24) (2019) 1902500.
[20] X. Wang, M. Niu, J. Fan, Q. Chen, X. Zhang, Nano Lett. 21 (2021) 4270–4279.
[21] H. Zhang, H. Liu, Z. Tian, D. Lu, Y. Yu, S. Cestellos-Blanco, K. Sakimoto, P. Yang, Nat. Nanotechnol. 13 (2018) 900–905.
[22] C. Wang, X. Nie, Y. Shi, Y. Zhou, J. Xu, X. Xia, H. Chen, ACS Nano 11 (2017) 5897–5905.
[23] J. Fan, Z. Li, X. Liu, D. Zheng, Y. Chen, X. Zhang, Nano Lett. 18 (2018) 2373–2380.
[24] T. Mokari, E. Rothenberg, I. Popov, R. Costi, U. Banin, Science 304 (2004) 1787–1790.
[25] X. Gu, Z. Xu, L. Gu, H. Xu, F. Han, B. Chen, X. Pan, Environ. Chem. Lett. 19 (2021) 167–187.
[26] J. Liu, Y. Zheng, Z. Hong, K. Cai, F. Zhao, H. Han, Sci. Adv. 2 (2016).
[27] B. Suganthan, N. Sekar, Y. Zhou, Y. Fang, R. Ramasamy, ECS Trans. 85 (2018) 1099.
[28] M. Sarma, S. Kaushik, P. Goswami, Biomass Bioenergy 90 (2016) 187–201.
[29] D. Lea-Smith, P. Bombelli, R. Vasudevan, C. Howe, Bba-Bioenergetics 1857 (2016) 247–255.
[30] P. Saura, D. Riepl, D. Frey, M. Wikstrom, V.I. Kaila, P Natl Acad Sci USA 119 (2022).
[31] S. Berrios-Rivera, G. Bennett, K. San, Metab. Eng. 4 (2002) 230.
[32] F. Gazzaniga, R. Stebbins, S. Chang, M. McPeek, C. Brenner, Microbiol Mol Biol R 73 (2009) 529.
[33] R. Zhu, D. Wang, Y. Zhang, J. Li, Chin. Sci. Bull. 51 (2006) 2611–2618.
[34] H. Ishikita, W. Saenger, J. Biesiadka, B. Loll, E.W. Knapp, P Natl Acad Sci USA 103 (2006) 9855–9860.
[35] H. Chang, S.T. Chew, M. Zheng, D. Lio, C. Wiraja, Y. Mei, X. Ning, M. Cui, A. Than, P. Shi, D. Wang, K. Pu, P. Chen, H. Liu, C. Xu, Nat. Biomed. Eng. 5 (2021) 1008–1018.
[36] M. Cui, M. Zheng, C. Wiraja, S.W.T. Chew, A. Mishra, V. Mayandi, R. Lakshminarayanan, C. Xu, Adv. Sci. 8 (2021) e2102327.

[37] J. Kim, M. Kim, H. Yang, K. Lee, H. Jung, J. Contr. Release 170 (2013) 430–436.
[38] D. Li, D. Hu, H. Xu, H. Patra, X. Liu, Z. Zhou, J. Tang, N. Slater, Y. Shen, Biomaterials 264 (2021) 120410.
[39] L. Liu, H. He, Z. Luo, H. Zhou, R. Liang, H. Pan, Y. Ma, L. Cai, Adv. Funct. Mater. 30 (2020).
[40] A.J. Monteith, J.M. Miller, C.N. Maxwell, W.J. Chazin, E.P. Skaar, Sci. Adv. 7 (37) (2021) eabj2101.
[[41]] F. Gong, J. Xu, B. Liu, N. Yang, L. Cheng, P. Huang, C. Wang, Q. Chen, C.F. Ni, Z. Liu, Chem-Us 8 (2022) 268.
[42] N. Yang, F. Gong, B. Liu, Y. Hao, Y. Chao, H. Lei, X. Yang, Y. Gong, X. Wang, Z. Liu, L. Cheng, Nat. Commun. 13 (2022) 2336.
[43] R. Zan, H. Wang, W. Cai, J. Ni, B.J.C. Luthringer-Feyerabend, W. Wang, H. Peng, W. Ji, J. Yan, J. Xia, Y. Song, X. Zhang, Bioact. Mater. 9 (2022) 385–396.